nature photonics

LETTERS

https://doi.org/10.1038/s41566-020-00725-3

Check for updates

Real-space observation of vibrational strong coupling between propagating phonon polaritons and organic molecules

Andrei Bylinkin[1,2], Martin Schnell[1,3], Marta Autore[1], Francesco Calavalle[1], Peining Li[1,4], Javier Taboada-Gutièrrez[5,6], Song Liu[7], James H. Edgar[7], Fèlix Casanova[1,3], Luis E. Hueso[1,3], Pablo Alonso-Gonzalez[5,6], Alexey Y. Nikitin[2,3] ✉ and Rainer Hillenbrand[3,8] ✉

Phonon polaritons in van der Waals materials can strongly enhance light–matter interactions at mid-infrared frequencies, owing to their extreme field confinement and long lifetimes[1–7]. Phonon polaritons thus bear potential for vibrational strong coupling with molecules. Although the onset of vibrational strong coupling was observed spectroscopically with phonon-polariton nanoresonators[8], no experiments have resolved vibrational strong coupling in real space and with propagating modes. Here we demonstrate by nanoimaging that vibrational strong coupling can be achieved between propagating phonon polaritons in thin van der Waals crystals (hexagonal boron nitride) and molecular vibrations in adjacent thin molecular layers. We performed near-field polariton interferometry, showing that vibrational strong coupling leads to the formation of a propagating hybrid mode with a pronounced anti-crossing region in its dispersion, in which propagation with negative group velocity is found. Numerical calculations predict vibrational strong coupling for nanometre-thin molecular layers and phonon polaritons in few-layer van der Waals materials, which could make propagating phonon polaritons a promising platform for ultrasensitive on-chip spectroscopy and strong-coupling experiments.

Phonon polaritons (PPs)—light coupled to lattice vibrations—in van der Waals (vdW) crystals open up new possibilities for infrared nanophotonics, owing to their strong infrared field confinement, picosecond-long lifetimes[1–7] and tunability via the crystal thickness and the dielectric environment[9–12]. Since PPs in many vdW materials spectrally coincide with molecular vibrational resonances, which abound the mid-infrared spectral range, PPs are thus promising candidates for achieving vibrational strong coupling (VSC) for developing ultrasensitive infrared spectroscopy and for modifying chemical properties of molecules[13–17]. Indeed, analogously to molecular vibrational infrared spectroscopy employing plasmons in graphene nanoribbons[18], localized PPs in high-*Q*-factor nanoresonators made of hexagonal boron nitride (h-BN) were recently coupled to molecular vibrations[8], allowing for ultrasensitive far-field spectroscopy at the strong-coupling limit. However, ultra-confined propagating PPs in unstructured layers have not been experimentally or theoretically explored for field-enhanced molecular vibrational spectroscopy. More generally, none of the ultra-confined propagating polaritons in a 2D material have been exploited so far experimentally for field-enhanced molecular vibrational spectroscopy, although theoretical studies predict intriguing on-chip spectroscopy applications[19]. Further, real-space nanoimaging of the hybrid modes has been elusive, although it is of fundamental importance for the in-depth experimental analysis of VSC exploiting PPs.

Here, we perform mid-infrared nanoimaging experiments[3–7] as a test bench to study the interaction of ultra-confined propagating PPs in vdW materials with molecular vibrations in sub-100 nm thick organic layers. Specifically, we perform phonon-polariton interferometry in thin, continuous h-BN layers interacting with 4,4′-bis(*N*-carbazolyl)-1,1′-biphenyl (CBP) molecules. In contrast to typical strong-coupling experiments, such as far-field spectroscopy in the Kretschmann–Raether configuration or of polariton nanoresonators, we monitor in real space the effect of molecular absorption on PPs, leading to a dramatic modification of the PP propagation length and anomalous dispersion with negative group velocity. We retrieve—in good agreement—experimentally and theoretically the quasi-normal modes of the CBP–PP coupled system, revealing considerable anti-crossing and mode splitting caused by strong coupling. A numerical study predicts that few-layer h-BN layers may enable strong coupling to be reached even in the case of atomically thin molecular layers, thus underlining the potential of PPs to become a platform for ultrasensitive on-chip spectroscopy devices.

In Fig. 1a we illustrate the PP interferometry experiment. We illuminate the metallic tip of a scattering-type scanning near-field optical microscope (s-SNOM) to launch PP modes in a thin h-BN layer, which is placed above a thin layer of CBP molecules. The tip-launched PPs propagate to the h-BN edge, reflect and propagate back to the tip. The resulting PP interference is shown in Fig. 1b by a numerical simulation of the electric field distribution along the h-BN–CBP layer. Importantly, the PP field penetrates into the molecular layer allowing for strong interaction between PPs and molecular vibrations. By mapping and analysing the PP interference

[1]CIC nanoGUNE BRTA, Donostia - San Sebastián, Spain. [2]Donostia International Physics Center (DIPC), Donostia - San Sebastián, Spain. [3]IKERBASQUE, Basque Foundation for Science, Bilbao, Spain. [4]Wuhan National Laboratory for Optoelectronics & School of Optical and Electronic Information, Huazhong University of Science and Technology, Wuhan, China. [5]Departamento de Fisica, Universidad de Oviedo, Oviedo, Spain. [6]Nanomaterials and Nanotechnology Research Center (CINN), El Entrego, Spain. [7]Tim Taylor Department of Chemical Engineering, Kansas State University, Manhattan, KS, USA. [8]CIC nanoGUNE BRTA and Department of Electricity and Electronics, UPV/EHU, Donostia - San Sebastián, Spain. ✉e-mail: alexey@dipc.org; r.hillenbrand@nanogune.eu

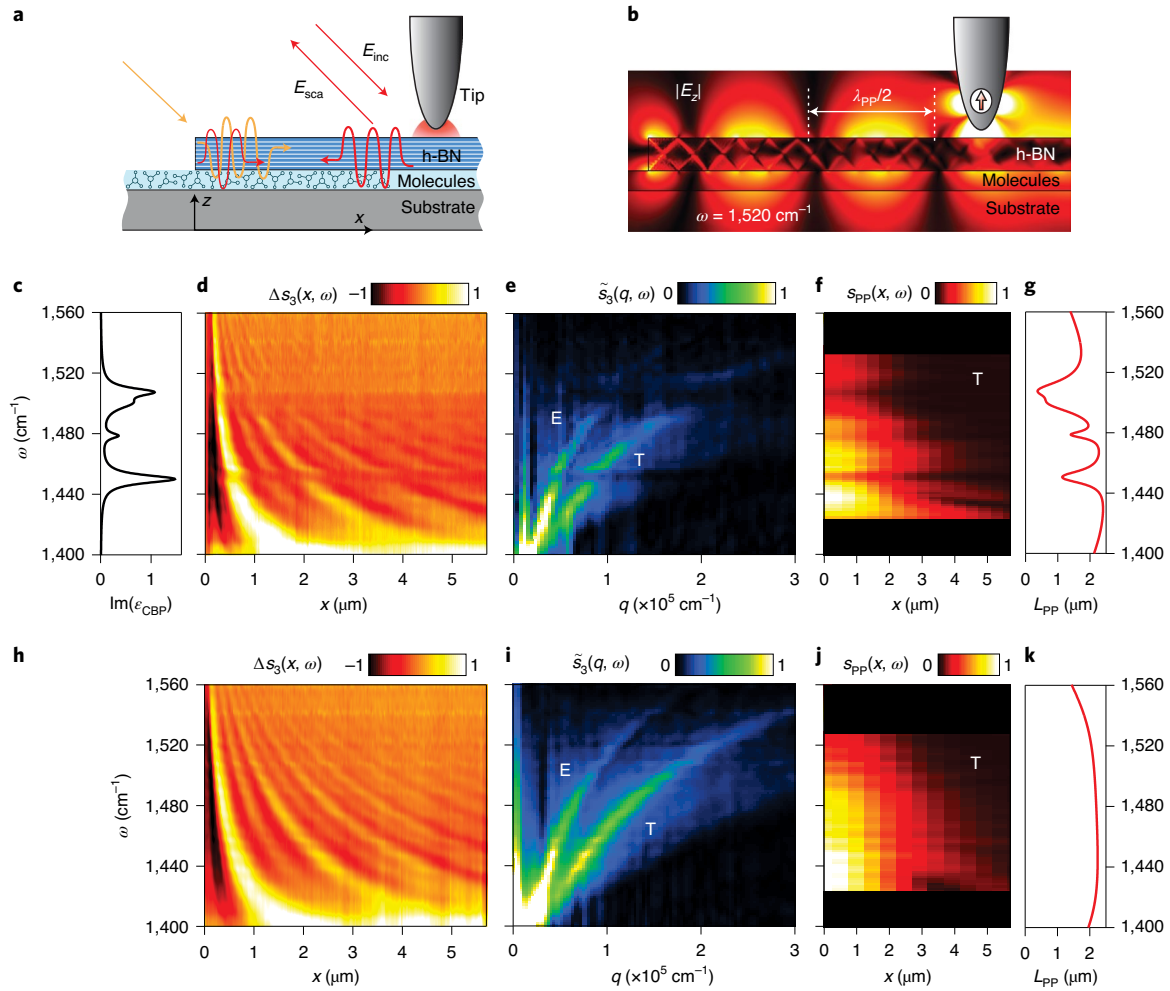

Fig. 1 | Phonon-polariton interferometry of molecular vibrations. a, Illustration of the nanoimaging experiment. E_{inc} and E_{sca} denote the electric field of the incident and tip-scattered radiation. The orange arrow indicates illumination of the h-BN edge. **b**, Simulated near-field distribution (magnitude of the z component of the electric field, E_z) generated by a point dipole source (vertical arrow) mimicking the illuminated tip. Outside the h-BN slab, it reveals essentially the interference of the fundamental PP slab mode (denoted M0), which is studied in this work. We note the appearance of a zigzag pattern inside the h-BN slab. It is formed by the superposition of higher-order slab modes, which are typical for vdW polar crystals[1,2,6,10]. They propagate with much larger momenta, and thus do not contribute to the coupling between the M0 mode and the molecular vibrations studied in this work. **c**, Imaginary part of the dielectric function ε_{CBP} of CBP molecules. **d**,**h**, Baseline-subtracted nano-FTIR amplitude signal $\Delta s_3(x, \omega)$ as a function of tip–edge distance x for h-BN–CBP (**d**) and pure h-BN (**h**) layers. **e**,**i**, Amplitude of the Fourier transform of **d** and **h**, respectively, along the x axis. E and T mark the M0 mode excited by the flake edge or tip, respectively. **f**,**j**, Isolated tip-scattered field of the M0 mode, obtained by an inverse Fourier transform of the filtered T branches (Supplementary Section II). **g**,**k**, Theoretical propagation length L_{PP} of the M0 mode. In **b**–**g**, the h-BN thickness is 50 nm, the CBP thickness is 40 nm and the substrate is 150 nm SiO_2 on Si. In **h**–**k**, the h-BN thickness is 50 nm and the substrate is 150 nm SiO_2 on Si.

spectroscopically, we can study how the molecule–PP interaction modifies the PP wavelength λ_{PP} and propagation length L_{PP}.

In a first experiment, we used Fourier transform infrared nanospectroscopy (nano-FTIR spectroscopy, see Methods) to record the tip-scattered field E_{sca} (which is governed by the PP interference) as a function of frequency ω and distance x between the tip and h-BN edge (Fig. 1d). We observe the typical signal oscillations (fringes) arising from the PP interference, whose period $\lambda_{PP}/2$ decreases with frequency ω (ref. [7]). Importantly, our data reveal interruptions of the fringes (strong reduction of the amplitude signals) at the frequencies of the molecular vibrational resonances (Fig. 1c), which are absent in the data obtained on h-BN layers without molecules (Fig. 1h), clearly indicating strong interaction between PPs and molecular vibrations.

To visualize the PP dispersion, we performed a Fourier transform of the PP interference pattern along the x axis, revealing two bright branches in the momentum–frequency, q–ω, domain (Fig. 1e and i for the h-BN–CBP and pure h-BN layers, respectively; see Supplementary Section II for the data processing details). As in previous experiments[6], both branches (labelled E and T) can be attributed to the fundamental PP slab mode (typically referred to as the M0 mode) launched by either the h-BN edge or the tip, respectively (Supplementary Fig. 4). The E branch directly reveals the momenta q of the M0 mode, in contrast to the T branch revealing $2q$, as the M0 mode propagates twice the distance x between the edge and the tip. We clearly see interruptions at the spectral position of the molecular vibrations, manifesting strong damping of the PPs by molecular absorption.

The strong interaction between molecular vibrations and PPs could lead to highly sensitive and ultracompact infrared spectroscopy devices. To briefly discuss this interesting aspect, we isolate the near-field signal of the tip-launched mode, $s_{PP}(x,\omega)$, by filtering, and

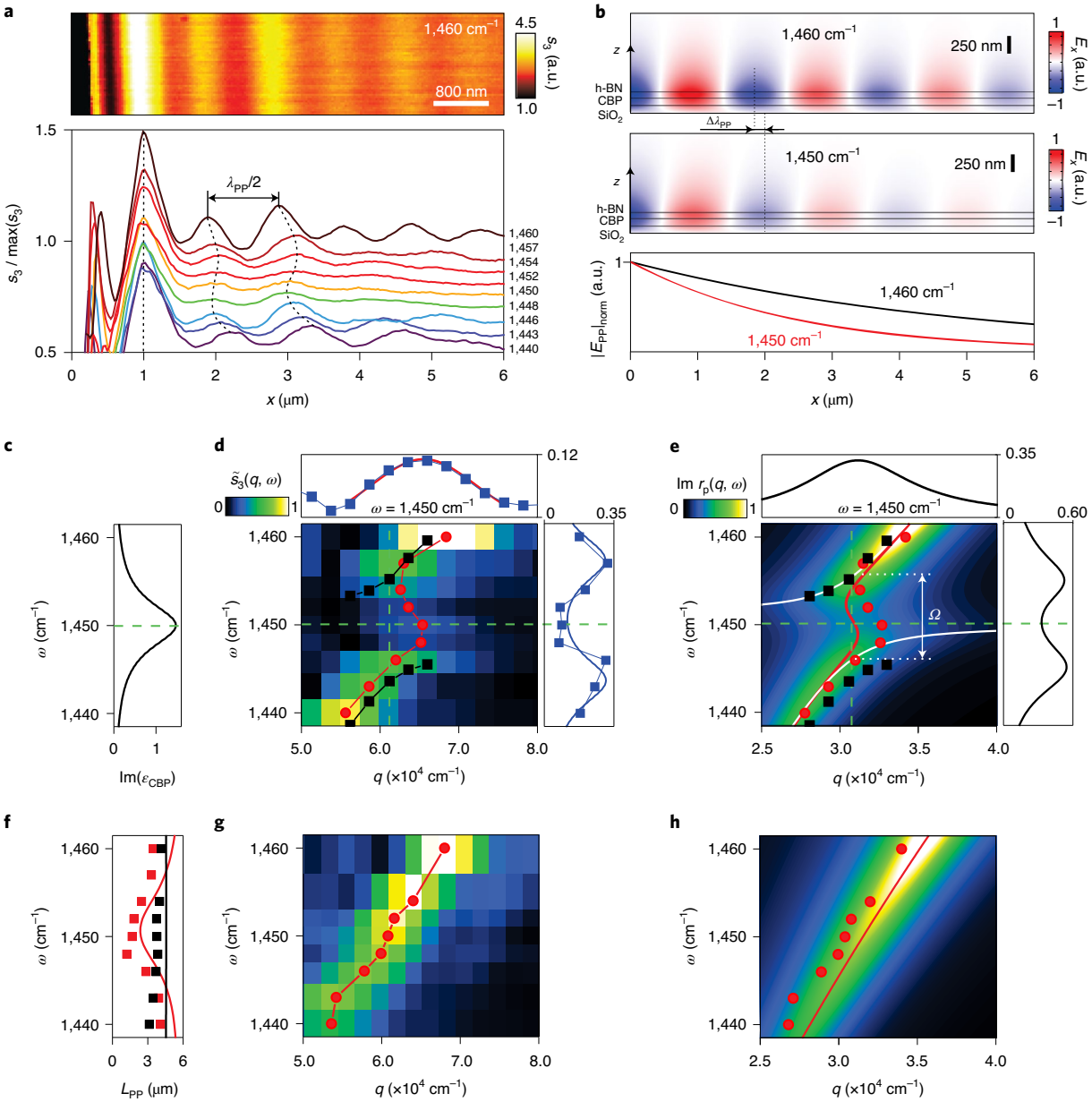

Fig. 2 | Real-space imaging of PPs on a h-BN–CBP layer in the region of anomalous dispersion. a, Top: infrared near-field amplitude image of an 85-nm-thick h-BN flake on a 100-nm-thick CBP layer at 1,460 cm^{-1}. Bottom: normalized amplitude profile perpendicular to the edge at different frequencies, extracted from images such as the one shown in the top panel. **b**, Top and middle: simulated near-field distribution (*x* component) of a PP mode propagating along the h-BN–CBP layer. Bottom: calculated absolute value of the PP field as a function of propagation distance *x*. **c**, Imaginary part of the dielectric function ε_{CBP} of CBP molecules. **d**, Colour plot showing the amplitude of the Fourier transform of the line profiles of panel **a**. **e**, Colour plot showing calculated imaginary part of the Fresnel reflection coefficient. Curves inside the colour plots show the calculated dispersions assuming complex-valued momentum (red) or complex-valued frequency (white). White arrow indicates mode splitting Ω. In **d** and **e**, the blue symbols and black curves in the right and top panels show line profiles along the dashed green vertical and horizontal lines, respectively. In **d**, the red curve in the top panel shows a Lorentz function fit and the blue curve in the right panel shows a coupled-oscillator fit. **f**, Experimental (symbols) and calculated (lines) propagation length L_{PP} of PPs on h-BN–CBP (red) and pure h-BN (black) layers. **g**,**h**, Same as for **d**,**e** (including colour scales) but for a h-BN layer without CBP.

directly reveal PP attenuation for each frequency ω (Fig. 1f,j and see Supplementary Section II for the data processing details). We observe that the PPs are less strongly excited and decay faster near the molecular vibrational resonances, demonstrating the possibility of detecting molecular vibrational signatures via the accumulated PP losses. The numerically calculated propagation lengths of the M0 mode in the presence and absence of the CBP layer (Fig. 1g and k, respectively) corroborate our experimental results qualitatively. We find a reduced propagation length at the CBP absorption bands (for example 0.5 μm at 1,510 cm^{-1}) compared with about 2 μm on pure h-BN.

To quantify the coupling between the molecule vibrations and PPs, we performed a second experiment with improved signal-to-noise ratio and spectral resolution. To that end, we imaged PPs on an 85-nm-thick h-BN layer above a 100-nm-thick CBP layer at various frequencies around the CBP vibration at 1,450 cm^{-1}

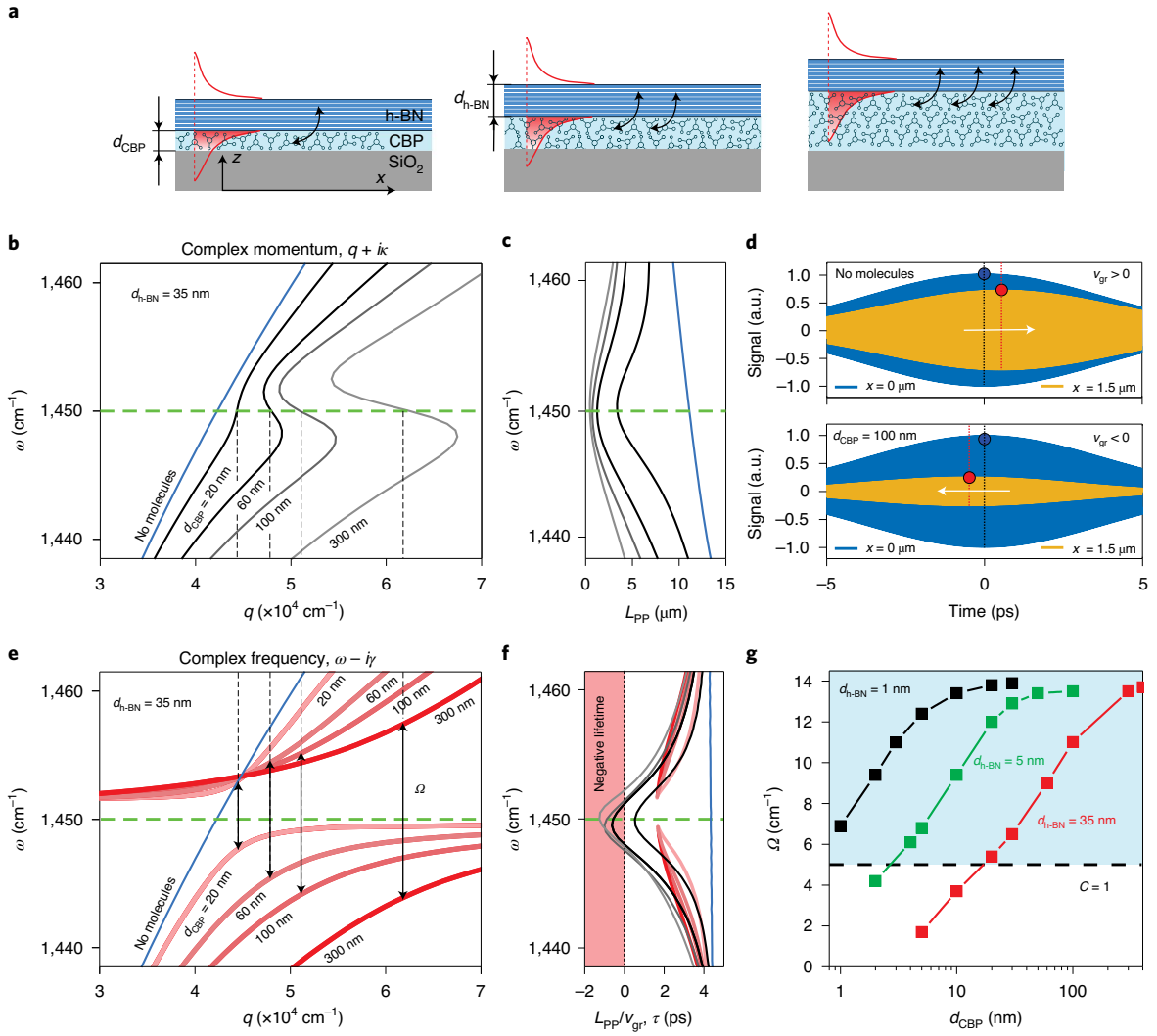

Fig. 3 | Dispersion and mode splitting. a, Illustration of PPs on molecular layers (CBP) of different thicknesses. Red lines illustrate the PP field. Red shaded areas mark the overlap between the PP field and molecules, which increases with CBP thickness, thus increasing the coupling strength between PPs and molecules as indicated by the black arrows. **b**,**e**, Dispersions of PPs in a 35-nm-thick h-BN layer on CBP layers of various thicknesses, d_{CBP}, obtained by eigenmode analysis via transfer matrix calculations assuming complex momenta $q + i\kappa$ (**b**) or complex frequencies $\omega - i\gamma$ (**e**). Horizontal green dashed line marks the frequency of the molecular vibrational resonance. **c**, PP propagation length. **d**, Narrowband PP pulses with 1,450 cm^{-1} centre frequency and 3.5 cm^{-1} spectral width at positions $x = 0$ and $x = 1.5$ μm in the absence (top) and presence (bottom) of a 100-nm-thick CBP layer below a 35-nm-thick h-BN layer. They exhibit positive and negative group velocity v_{gr}, respectively, as recognized by comparing the pulse maxima (marked by blue and red symbols) and their evolution with time (indicated by the white arrows). **f**, Blue and red lines show PP lifetime according to $\tau = 1/\gamma$. Black and grey lines show L_{PP}/v_{gr}. **g**, Mode splitting Ω as a function of the molecular layer thickness d_{CBP} for a h-BN layer with thickness $d_{h\text{-}BN}$ of 1 nm (black), 5 nm (green) and 35 nm (red). Horizontal black dashed line indicates the strong-coupling limit.

(Fig. 2c) employing a quantum cascade laser (Fig. 2a, top; see Methods). From the images, we extracted line profiles (Fig. 2a, bottom; see Methods), which show anomalous dispersion[20–22] near the CBP resonance. We clearly see that the PP wavelength λ_{PP} increases as the molecular resonance is crossed from 1,446 to 1,454 cm^{-1} (indicated by black dashed lines in Fig. 2a). To analyse the corresponding dispersion, we assembled Fourier transforms of the line profiles into a $\tilde{s}_3(q, \omega)$ plot (Fig. 2d and see Supplementary Section III for the data processing details). By fitting the $\tilde{s}_3(q, \omega)$ in the q direction using a Lorentz function and marking the maxima (red symbols in Fig. 2d), we clearly see that molecular absorption introduces a back bending in the PP dispersion, in stark contrast to the PP dispersion observed for h-BN without molecules (Fig. 2g, obtained analogously to Fig. 2d for the pure h-BN layer). Further, the propagation length is strongly reduced by the presence of molecules (red symbols in Fig. 2f). Both observations represent a fundamental landmark feature of a strong interaction between a propagating mode and a dipolar excitation, here observed in real space for ultra-confined PPs coupled to molecular vibrations (which may be named phovibrons). The near-field simulation shown in Fig. 2b confirms the reduction of the propagation length when the frequency decreases from 1,460 to 1,450 cm^{-1}.

The considerable back bending of the dispersion indicates strong coupling between the PPs and the molecular vibrations of CBP, which in the following we corroborate by quasi-normal mode analysis. To this end, we extracted $\tilde{s}_3(\omega)$ line profiles from Fig. 2d for fixed momenta q and fitted the data with a coupled-oscillator model[8,23,24] (Supplementary Section IV), yielding the dispersion of the quasi-normal modes, $\omega_{\pm}(q)$ (black symbols in Fig. 2d)[25]. The right panel of Fig. 2d shows, by way of an example, the experimental

line profile (blue symbols) and coupled-oscillator fit (blue line) for the q value marked by the vertical dashed line in the $\tilde{s}_3(q,\omega)$ plot. We observe a clear anti-crossing behaviour of the quasi-normal modes at the CBP resonance and a mode splitting of $\Omega = 11\,\mathrm{cm}^{-1}$. Considering the uncoupled PP and CBP linewidths of $\Gamma_{\mathrm{PP}} = 8\,\mathrm{cm}^{-1}$ (taking into account the SiO_2/Si substrate) and $\Gamma_{\mathrm{CBP}} = 6.4\,\mathrm{cm}^{-1}$, respectively (Methods and Supplementary Sections I and IV), we find that the strong-coupling condition $C \equiv \frac{\Omega^2}{\left(\frac{\Gamma_{\mathrm{CBP}}^2}{2}+\frac{\Gamma_{\mathrm{PP}}^2}{2}\right)} = 2.3 > 1$ is well fulfilled[26].

To interpret the $\tilde{s}_3(q,\omega)$ data and to verify the extracted experimental dispersions, we performed a theoretical eigenmode analysis. To that end, we calculated the Fresnel reflection coefficient, r_{p}, of h-BN–CBP and pure h-BN layers on a SiO_2/Si substrate employing the transfer matrix method[27] (see Methods). We find that the $\mathrm{Im}(r_{\mathrm{p}})$ plotted as a function of real q and ω (Fig. 2e,h) describes well the experimental data $\tilde{s}_3(q,\omega)$ (Fig. 2d,g), particularly peak positions, linewidths and the saddle point at the CBP resonance, demonstrating that spatially Fourier transformed spectral polariton interferometry can be interpreted analogously to momentum- and frequency-resolved surface plasmon resonance spectroscopy employing, for example, the classical Kretschmann–Raether configuration[26,28–31].

To obtain the eigenmode dispersions, we determined the poles of r_{p}, assuming either complex momenta $q + i\kappa$ (corresponding to spatially decaying modes with propagation length $L_{\mathrm{PP}} = 1/\kappa$) or complex frequencies $\omega - i\gamma$ (corresponding to temporally decaying modes with lifetime $\tau = 1/\gamma$). For spatially decaying modes in h-BN–CBP layers, we find a continuous dispersion exhibiting back bending (compare red curve in Fig. 2e with red curve in Fig. 2h showing results for the pure h-BN layer) and reduced propagation lengths L_{PP} around the CBP resonance (compare red curve in Fig. 2f with black curve showing L_{PP} for the pure h-BN layer). In contrast, analysis of temporally decaying modes yields quasi-normal modes featuring anti-crossing (white curves in Fig. 2e) and mode splitting of $\Omega = 10\,\mathrm{cm}^{-1}$, which according to $C = 1.9$ indicates strong coupling. The excellent agreement between experimental dispersions and propagation lengths (solid lines versus symbols in Fig. 2e,f) clearly demonstrates the unique capability of polariton interferometry for comprehensive and quantitative analysis of the coupling between ultra-confined propagating polaritons and dipolar excitations, here specifically revealing strong coupling between propagating PPs and molecular vibrations.

We deepen the insights into strong coupling between molecular vibrations and PPs by an eigenmode analysis via transfer matrix calculations (analogous to Fig. 2e) for various h-BN and CBP layer thicknesses. We first consider a variation of the CBP layer thickness d_{CBP} for a fixed h-BN thickness of 35 nm (Fig. 3b–f). We find that the region of anomalous dispersion widens when d_{CBP} is increased, which is accompanied by a reduction of the PP propagation length L_{PP} (that is, increase of PP damping) that reaches a finite minimum at the molecular resonance (Fig. 3c). Further, we find that with increasing d_{CBP} the mode splitting Ω (the smallest vertical separation between the real frequency of the quasi-normal modes) and thus the coupling strength between PPs and molecular vibrations increases (Fig. 3e), as simply more of the PP field lies inside the CBP layer (Fig. 3a). Interestingly, the lifetimes are rather large, about 2 ps, for all considered d_{CBP} (red curves in Fig. 3f, obtained from the eigenmode analysis described above), which is close to the molecular resonance lifetime of 1.7 ps and emphasizes that the coupled mode becomes more determined by the character of molecular absorption near the resonance. We note that the lifetime of the coupled mode being slightly longer than the lifetime of the bare molecular excitation has also been found by real-space observation of exciton polaritons[32]. In the region of anomalous dispersion the PPs propagate with negative group velocity, $v_{\mathrm{g}} = \mathrm{d}\omega/\mathrm{d}q < 0$ (Fig. 2d and Fig. 3b), yet with finite propagation length (red symbols in Fig. 2f and Fig. 3c). A simulation of the decay of narrowband PP pulses illustrates this effect (Fig. 3d). In the presence of a molecular layer, we find that the maximum of the pulse envelope after propagation of $x = 1.5$ μm appears at negative times t. Importantly, the negative group velocity yields negative values for the lifetime τ when calculated according to $\tau = L_{\mathrm{PP}}/v_{\mathrm{g}}$ (black curves in Fig. 3f), implying that this lifetime determination—typically applied in polariton interferometry[3,4,6,33,34]—cannot be used in the case of anomalous dispersion. Instead, eigenmode analysis in the picture of a temporally decaying mode is required (red curves in Fig. 3f).

Plotting Ω as a function of d_{CBP}, we find saturation at about $14\,\mathrm{cm}^{-1}$ for $d_{\mathrm{CBP}} > 300$ nm (red symbols in Fig. 3g), where the whole PP lies inside the CBP layer. Considering that the condition $C > 1$ in our simulations is fulfilled for $\Omega > 5\,\mathrm{cm}^{-1}$ (Supplementary Section V), we find that strong coupling of CBP vibrations and PPs in a 35-nm-thick h-BN layer can be achieved for $d_{\mathrm{CBP}} > 20$ nm. Remarkably, further numerical mode analysis for h-BN layers with reduced thickness of $d_{\text{h-BN}} = 5$ nm and 1 nm (green and black symbols in Fig. 3g, respectively) predicts that in future experiments strong coupling may be achieved with just a few CBP monolayers ($d_{\mathrm{CBP}} < 2$ nm). This can be explained by the extreme mode compression that is a consequence of the 100-fold reduced PP wavelength compared with the photon wavelength of the same energy[35].

Our work demonstrates that propagating PPs in unstructured vdW materials can strongly couple to molecular vibrations, which could provide a platform for testing strong coupling and the local control of chemical properties[13–16]. In addition, it opens up the possibility for ultracompact, on-chip spectroscopy[19]. A large variety of vdW materials are available to go beyond the spectral range of h-BN, as recently demonstrated by PP observation on MoO_3 (ref. [4]) and V_2O_5 (ref. [33]). In contrast to conventional polaritonic spectroscopy conducted with resonators (for example, ribbons[8], cones[36] or hole arrays[37]), our work opens new avenues for studying strong light–matter interactions without the need for challenging sample structuring that typically is accompanied by additional losses from sample damage, inhomogeneities and scattering due to uncertainties in the sample fabrication process.

Online content

Any methods, additional references, Nature Research reporting summaries, source data, extended data, supplementary information, acknowledgements, peer review information; details of author contributions and competing interests; and statements of data and code availability are available at https://doi.org/10.1038/s41566-020-00725-3.

Received: 24 July 2020; Accepted: 20 October 2020;
Published online: 23 November 2020

References

1. Basov, D. N., Fogler, M. M. & García De Abajo, F. J. Polaritons in van der Waals materials. *Science* **354**, aag1992 (2016).
2. Low, T. et al. Polaritons in layered two-dimensional materials. *Nat. Mater.* **16**, 182–194 (2017).
3. Giles, A. J. et al. Ultralow-loss polaritons in isotopically pure boron nitride. *Nat. Mater.* **17**, 134–139 (2018).
4. Ma, W. et al. In-plane anisotropic and ultra-low-loss polaritons in a natural van der Waals crystal. *Nature* **562**, 557–562 (2018).
5. Zheng, Z. et al. Highly confined and tunable hyperbolic phonon polaritons in van der Waals semiconducting transition metal oxides. *Adv. Mater.* **30**, e1705318 (2018).
6. Yoxall, E. et al. Direct observation of ultraslow hyperbolic polariton propagation with negative phase velocity. *Nat. Photon.* **9**, 674–678 (2015).
7. Dai, S. et al. Tunable phonon polaritons in atomically thin van der Waals crystals of boron nitride. *Science* **343**, 1125–1129 (2014).
8. Autore, M. et al. Boron nitride nanoresonators for phonon-enhanced molecular vibrational spectroscopy at the strong coupling limit. *Light Sci. Appl.* **7**, 17172–17178 (2018).

9. Dai, S. et al. Graphene on hexagonal boron nitride as a tunable hyperbolic metamaterial. *Nat. Nanotechnol.* **10**, 682–686 (2015).
10. Kim, K. S. et al. The effect of adjacent materials on the propagation of phonon polaritons in hexagonal boron nitride. *J. Phys. Chem. Lett.* **8**, 2902–2908 (2017).
11. Fali, A. et al. Refractive index-based control of hyperbolic phonon-polariton propagation. *Nano Lett.* **19**, 7725–7734 (2019).
12. Dai, S. et al. Hyperbolic phonon polaritons in suspended hexagonal boron nitride. *Nano Lett.* **19**, 1009–1014 (2019).
13. Thomas, A. et al. Tilting a ground-state reactivity landscape by vibrational strong coupling. *Science* **363**, 615–619 (2019).
14. Herrera, F. & Owrutsky, J. Molecular polaritons for controlling chemistry with quantum optics. *J. Chem. Phys.* **152**, 100902 (2020).
15. Thomas, A. et al. Ground-state chemical reactivity under vibrational coupling to the vacuum electromagnetic field. *Angew. Chem. Int. Ed. Engl.* **128**, 11634–11638 (2016).
16. Ribeiro, R. F., Martínez-Martínez, L. A., Du, M., Campos-Gonzalez-Angulo, J. & Yuen-Zhou, J. Polariton chemistry: controlling molecular dynamics with optical cavities. *Chem. Sci.* **9**, 6325–6339 (2018).
17. Feist, J., Galego, J. & Garcia-Vidal, F. J. Polaritonic chemistry with organic molecules. *ACS Photonics* **5**, 205–216 (2018).
18. Rodrigo, D. et al. Mid-infrared plasmonic biosensing with graphene. *Science* **349**, 165–168 (2015).
19. Francescato, Y., Giannini, V., Yang, J., Huang, M. & Maier, S. A. Graphene sandwiches as a platform for broadband molecular spectroscopy. *ACS Photonics* **1**, 437–443 (2014).
20. Hu, F. et al. Imaging exciton–polariton transport in $MoSe_2$ waveguides. *Nat. Photon.* **11**, 356–360 (2017).
21. Arakawa, E. T., Williams, M. W., Hamm, R. N. & Ritchie, R. H. Effect of damping on surface plasmon dispersion. *Phys. Rev. Lett.* **31**, 1127–1129 (1973).
22. Schuller, E., Falge, H. J. & Borstel, G. Dispersion curves of surface phonon-polaritons with backbending. *Phys. Lett. A* **54**, 317–318 (1975).
23. Novotny, L. Strong coupling, energy splitting, and level crossings: a classical perspective. *Am. J. Phys.* **78**, 1199–1202 (2010).
24. Wu, X., Gray, S. K. & Pelton, M. Quantum-dot-induced transparency in a nanoscale plasmonic resonator. *Opt. Express* **18**, 23633–23645 (2010).
25. Hennessy, K. et al. Quantum nature of a strongly coupled single quantum dot–cavity system. *Nature* **445**, 896–899 (2007).
26. Törmö, P. & Barnes, W. L. Strong coupling between surface plasmon polaritons and emitters: a review. *Rep. Prog. Phys.* **78**, 13901 (2015).
27. Passler, N. C. & Paarmann, A. Generalized 4 × 4 matrix formalism for light propagation in anisotropic stratified media: study of surface phonon polaritons in polar dielectric heterostructures. *J. Opt. Soc. Am. B* **34**, 2128–2139 (2017).
28. Pockrand, I., Brillante, A. & Möbius, D. Exciton-surface plasmon coupling: an experimental investigation. *J. Chem. Phys.* **77**, 6289–6295 (1982).
29. Bellessa, J., Bonnand, C., Plenet, J. C. & Mugnier, J. Strong coupling between surface plasmons and excitons in an organic semiconductor. *Phys. Rev. Lett.* **93**, 036404 (2004).
30. Memmi, H., Benson, O., Sadofev, S. & Kalusniak, S. Strong coupling between surface plasmon polaritons and molecular vibrations. *Phys. Rev. Lett.* **118**, 126802 (2017).
31. Shlesinger, I. et al. Strong coupling of nanoplatelets and surface plasmons on a gold surface. *ACS Photonics* **6**, 2643–2648 (2019).
32. Rozenman, G. G., Akulov, K., Golombek, A. & Schwartz, T. Long-range transport of organic exciton-polaritons revealed by ultrafast microscopy. *ACS Photonics* **5**, 105–110 (2018).
33. Taboada-Gutiérrez, J. et al. Broad spectral tuning of ultra-low-loss polaritons in a van der Waals crystal by intercalation. *Nat. Mater.* **19**, 964–968 (2020).
34. Bezares, F. J. et al. Intrinsic plasmon-phonon interactions in highly doped graphene: a near-field imaging study. *Nano Lett.* **17**, 5908–5913 (2017).
35. Dai, S. et al. Phonon polaritons in monolayers of hexagonal boron nitride. *Adv. Mater.* **31**, 1806603 (2019).
36. Caldwell, J. D. et al. Sub-diffractional volume-confined polaritons in the natural hyperbolic material hexagonal boron nitride. *Nat. Commun.* **5**, 5221 (2014).
37. Alfaro-Mozaz, F. J. et al. Deeply subwavelength phonon-polaritonic crystal made of a van der Waals material. *Nat. Commun.* **10**, 42 (2019).

Methods

Sample preparation. 4,4′-bis(*N*-carbazolyl)-1,1′-biphenyl with sublimed quality (99.9%) (Sigma-Aldrich, Saint Louis, MO, USA) was thermally evaporated in an ultra-high-vacuum evaporator chamber (base pressure $<10^{-9}$ mbar) at a rate of 0.1 nm s^{-1} using a Knudsen cell.

The h-BN crystal flake was grown from a metal flux at atmospheric pressure as described previously[38]. The thin layers used in this study were prepared by mechanical exfoliation with blue Nitto tape. Then, we performed a second exfoliation of the h-BN flakes from the tape onto a transparent polydimethylsiloxane stamp. Using optical inspection of the h-BN flakes on the stamp, we identified high-quality flakes with appropriate thickness. These flakes were transferred onto a Si/SiO_2/CBP substrate using the deterministic dry transfer technique.

Nano-FTIR spectroscopy. We used a commercial s-SNOM set-up equipped with a nano-FTIR module (Neaspec GmbH, Martinsried, Germany), in which the oscillating (at a frequency $\Omega \cong 270$ kHz) metal-coated (Pt/Ir) atomic force microscope tip (Arrow-NCPt-50, Nanoworld, Nano-World AG, Neuchâtel, Switzerland) was illuminated by *p*-polarized broadband mid-infrared radiation generated by a supercontinuum laser (Femtofiber pro IR and SCIR; Toptica, Gräfelfing, Germany; average power of about 0.5 mW; frequency range 1,200–1,700 cm^{-1}). The spectral resolution was set to 6.25 cm^{-1}, which is the limit of the set-up. The spatial step (pixel) size in the nano-FTIR line scan shown in Fig. 1d is 20 nm, the total scan length is 6 μm and the number of pixels is 300. In Fig. 1h, the pixel size is 27 nm, the total scan length is 8 μm and the number of pixels is 300. To suppress background scattering from the tip shaft and sample, the detector signal was demodulated at a frequency 3Ω. The complex-valued nano-FTIR spectra (expressed by amplitude and phase, s_3 and φ_3, respectively) were normalized to the spectra of the Si substrate, $s_3(x,\omega)e^{i\varphi_3(x,\omega)} = s_3^{\mathrm{h-BN-CBP}}(x,\omega)e^{i\varphi_3^{\mathrm{h-BN-CBP}}(x,\omega)}/s_3^{\mathrm{Si}}(\omega)e^{i\varphi_3^{\mathrm{Si}}(\omega)}$.

Infrared nanoimaging by s-SNOM employing quantum cascade laser illumination. The oscillating tip (same parameters as described in the 'Nano-FTIR spectroscopy' section) was illuminated by *p*-polarized mid-infrared radiation from a wavelength-tunable quantum cascade laser. The backscattered light was collected with a pseudo-heterodyne interferometer. To suppress background scattering from the tip shaft and sample, the detector signal was demodulated at a frequency 3Ω.

The top panel in Fig. 2a shows a representative near-field amplitude image, s_3, of an 80-nm-thick h-BN flake above a 100-nm-thick CBP layer at $\omega = 1{,}460$ cm^{-1}. By imaging the same sample area at various frequencies and averaging them in the direction parallel to the h-BN edge, we obtained the near-field line profiles shown in the bottom panel in Fig. 2a.

Eigenmode analysis. We used the transfer matrix approach to calculate the PP eigenmodes[27]. They can be found by determining the poles in the Fresnel reflectivity of the layered sample for *p*-polarized light, r_p. To determine the poles, we numerically solved the equation $1/\mathrm{Abs}(r_p) = 0$. For spatially decaying modes, we considered complex momenta $q + i\kappa$ and real-valued ω, and determined the poles of $r_p(q+i\kappa, \omega)$, yielding $\omega(q)$ and the propagation length $L_{PP} = 1/\kappa$. For temporally decaying modes, we considered complex frequencies $\omega - i\gamma$ and real-valued q, and determined the poles of $r_p(q, \omega-i\gamma)$, yielding $\omega(q)$, lifetime $\tau = 1/\gamma$, and the mode linewidth $\Gamma = \gamma/2$. The dielectric permittivity of h-BN, CBP, Si and SiO_2 were modelled as described in Supplementary Section I.

Electromagnetic simulations. Full-wave numerical simulations using the finite-element method in the frequency domain (COMSOL) were performed to study the electric field distribution around the h-BN–CBP heterostructure on top of a Si/SiO_2 substrate. The dielectric permittivity of h-BN, CBP, Si and SiO_2 were modelled as described in Supplementary Section I.

Data availability

The data that support the plots within this paper and other findings of this study are available from the corresponding authors on reasonable request.

References

38. Liu, S. et al. Single crystal growth of millimeter-sized monoisotopic hexagonal boron nitride. *Chem. Mater.* **30**, 6222–6225 (2018).

Acknowledgements

We thank R. Esteban and J. Aizpurua for discussions. We acknowledge financial support from the Spanish Ministry of Science, Innovation and Universities (national projects MAT2017-88358-C3, RTI2018-094830-B-100, RTI2018-094861-B-100, and the project MDM-2016-0618 of the Maria de Maeztu Units of Excellence Program), the Basque Government (grant numbers IT1164-19 and PIBA-2020-1-0014) and the European Union's Horizon 2020 research and innovation programme under the Graphene Flagship (grant agreement numbers 785219 and 881603, GrapheneCore2 and GrapheneCore3). F. Calavelle acknowledges support from the European Union H2020 under the Marie Skłodowska-Curie Actions (766025-QuESTech). J.T.-G. acknowledges support through the Severo Ochoa Program from the Government of the Principality of Asturias (number PA-18-PF-BP17-126). P.A.-G. acknowledges support from the European Research Council under starting grant number 715496, 2DNANOPTICA. Further, support from the Materials Engineering and Processing program of the National Science Foundation, award number CMMI 1538127 for h-BN crystal growth is greatly appreciated.

Author contributions

R.H. and M.A. conceived the study with the help of A.B. and A.Y.N. Sample fabrication was performed by A.B. and F. Calavelle, supervised by F. Casanova and L.E.H. A.B. performed the experiments, data analysis and simulations. M.A., M.S. and J.T.-G. contributed to the near-field imaging experiments. M.A. and M.S. participated in the data analysis. P.L. contributed to simulations. S.L. and J.H.E. grew the isotopically enriched boron nitride. R.H. and A.Y.N. supervised the work. R.H., M.S. and A.B. wrote the manuscript with the input of A.Y.N., P.A.-G. and M.A. All authors contributed to scientific discussion and manuscript revisions.

Competing interests

R.H. is co-founder of Neaspec GmbH, a company producing scattering-type scanning near-field optical microscope systems, such as the one used in this study. The remaining authors declare no competing interests.

Additional information

Supplementary information is available for this paper at https://doi.org/10.1038/s41566-020-00725-3.

Correspondence and requests for materials should be addressed to A.Y.N. or R.H.

Peer review information *Nature Photonics* thanks the anonymous reviewers for their contribution to the peer review of this work.

Reprints and permissions information is available at www.nature.com/reprints.